Thermohydraulic experiments on a supercritical carbon dioxide - air microtube heat exchanger

Kaiyuan Jin*, Akshay Bharadwaj Krishna, Zachary Wong, Portonovo S. Ayyaswamy, Ivan Catton, Timothy S. Fisher*

Mechanical and Aerospace Engineering Department, University of California, Los Angeles, CA 90095, USA

* Corresponding authors: Kaiyuan Jin (kaiyuanj@ucla.edu), Timothy S. Fisher (tsfisher@ucla.edu)

Abstract: Heat exchangers are critical components in supercritical CO_2 Brayton cycles and provide necessary heat input, recovery, and dissipation. Tubular heat exchangers with unconventionally small tube sizes (tube diameters less than 5 mm) are promising components for supercritical CO_2 cycles and potentially provide excellent structural stability with wide scope of application. This paper provides essential design and fabrication guidelines for a compact shell-and-tube heat exchanger with microtubes (with an inner diameter equal to 1.75 mm). A heat exchanger test rig is used to evaluate the thermohydraulic performance of this heat exchanger with supercritical CO_2 and air as working fluids. Thermohydraulic data are reported for more than forty sets of experiments with varying Reynolds numbers for shell and tube flows. Critical performance metrics are calculated from the data and compared with predictions from a previously described numerical model. The average deviations between the experimental and model results fall within 10% for all critical metrics. This excellent agreement validates the numerical model for supercritical CO_2 heat exchanger optimization and scale-up.

Keywords: Supercritical CO_2, shell-and-tube heat exchanger, microtube, thermohydraulics, thermal conductance, friction factor

1. INTRODUCTION

Increasing the capacity and efficiency of energy conversion processes is critical to alleviate worldwide energy and environmental challenges and support global economic development. Supercritical CO_2 (sCO_2) has become a promising working fluid candidate for future energy infrastructure due to its favorable hydrodynamic properties [1,2], high density [2,3], and excellent material compatibility [1,3]. Using sCO_2 for thermal power generation enables higher thermal efficiencies [4,5] and more compact footprints than the conventional power generation cycles, such as the air Brayton cycle and the steam Rankine cycle. Many sCO_2 thermal cycle designs have been proposed to generate electricity with increased efficiencies while reducing system size, water consumption, and capital and operating costs for future applications of nuclear power [6,7], concentrated solar power (CSP) [8,9], and waste heat to power (WHP) [10,11].

Heat exchangers (HXs) are indispensable components in advanced sCO_2 cycle systems and provide necessary heat acquisition, transport, and recuperation to promote thermal efficiency [2,12]. Operating at much higher temperatures and pressures, sCO_2 HXs have higher energy density and more compact footprints compared to conventional HXs. Plate HXs with micro-scale channels generally have the smallest footprints and therefore are an important HX type for sCO_2 applications [13,14]. Among plate HXs, printed circuit HXs (PCHXs) have gained particular attention for their high heat transfer capacity [18], long-term structural integrity [19], and attractive power density [15-17]. In addition to original straight-channel PCHXs, advanced flow channel designs including zigzag [18,19], finned [20,21], and wavy [22,23] configurations have been proposed in recent years to achieve high performance metrics. Cheng et al. [24] and Park et al. [25] reported HX test rigs to characterize thermohydraulic performance of PCHXs for precooling in the sCO_2 Brayton cycle. Chu et al. [26] elucidated the effects of critical design parameters of zigzag channels on HX performance through a series of tests on a small-scale sCO_2 PCHX. Chang et al. [27] performed an experimental investigation on the thermohydraulics of airfoil-fin PCHXs with sCO_2 near the pseudo-critical point. These experimental studies provide the necessary design basis for future scaled-up PCHX applications.

Tubular HXs, including shell-and-tube HXs (STHXs) [28,29], finned tube HXs [30,31], and tube-in-tube HXs [32] are also promising candidates for sCO_2 power generation cycles. These configurations are generally versatile and can withstand extreme operating conditions, largely because the circular flow boundaries in tubular HXs have excellent structural stability at high temperatures and pressures

[33,34]. However, most existing tubular HXs have large footprint because the tube diameters are usually of relatively large scale (> 5 mm) [35]. To achieve higher component power densities and more compact sizes, micro-scale tubes (with inner diameters of 0.5-3 mm) can be utilized, and relevant microtube HX technologies need to be developed further for sCO_2 applications.

The first sCO_2 microtube HX was proposed and fabricated by Thar Energy LLC in 2017 [29]. Using tubes of ~ 1mm diameter, several HX prototypes with a single flow path achieved a similar heat transfer area density to PCHXs (≈1800 m^2/m^3). A relevant thermohydraulic performance model was also developed based on existing Dittus-Boelter correlations and Colebrook-White equations. In recent years, multi-path HXs using microtubes, namely microtube STHXs (MT-STHXs), have gained interest, and multiple efforts have been reported to characterize their complex thermohydraulic behavior. Jiang et al. [36] developed a MT-STHX design model and provided optimal designs for recuperative HXs (recuperators) in a 10MWe sCO_2 Brayton cycle. Chai and Tassou [37,38] modeled both PCHXs and MT-STHXs based on standard correlations and showed that the latter can potentially achieve lower pressure drop on the sCO_2 side. Cai et al. conducted both numerical [39] and experimental [40] studies for sCO2-water MT-STHXs with low Reynolds numbers (⩽3000) and discussed the effects of design parameters such as baffle spacing on overall heat exchanger performance. Krishna et al. provided original correlations [41] for multiple tube bank configurations at high Reynolds numbers (3000-15000) and developed a 2D numerical model for designing [42] and optimizing [43] MT-STHXs with sCO_2. These studies provide important insights for the advancement of MT-STHX technologies. However, unlike PCHXs, experimental data for such HXs with sCO_2 as a working fluid remain scarce, especially for high Reynolds number conditions. New test data are needed to validate and improve the existing models and to provide a design framework for MT-STHXs.

To address the challenges above, this paper reports an original experimental study on a fabricated MT-STHX with sCO_2 and air as the working fluids. The HX consists of thirty-nine microtubes (ID = 1.75mm), 5 unit-cells and similar design features to future commercial-scale sCO_2 HXs. The integrated experimental system allows detailed analysis of thermohydraulic behavior in the HX at high Reynold number ranges that have not been experimentally studied in prior work. Performance metrics for multiple sCO_2 and air flow rates are obtained, and entrance and exit effects for shell-side flow are quantified. Finally, a numerical model developed by Krishna et al. [41,42] is applied to

predict performance for all experimental cases with good overall agreement between modeling and experimental results.

2. EXPERIMENTAL FACILITY

2.1. sCO_2 HX experimental system

A rig was developed to perform high-temperature thermohydraulic tests on sCO_2 HXs. As shown in Figure 1, the system consists of a closed sCO_2 loop manufactured by Accudyne System, Inc. (components connected by blue pipelines), an air loop (components connected by orange pipelines), a fabricated MT-STHX, and a data acquisition sub-system. The sCO_2 loop provides the test section with sCO_2 flow at 100 bar using a 1kW CO_2 pump assisted by a CO_2 pressure regulator and relief valve. The flow rate can be varied from 12 to 25 g/s and is controlled by the pump speed. The pressurized CO_2 flow is heated by a 2.5 kW PID-controlled heater. The heater outlet temperature can be controlled between 50 and 200 ^oC within $\pm 0.1^oC$, thus maintaining the CO_2 at the supercritical state. A commercial recuperator is installed to preheat the sCO_2 flow and minimize the required heater power. The heated flow is cooled down by a 7.5kW chiller before returning to the CO_2 pump to prevent cavitation. Within the air loop, flow is provided by a rotary air compressor, and the flow rate is controlled by a controller ranging from 5 to 45 g/s. A 6 kW air heater can heat the flow up to 300 ^oC before entering the HX. During an experiment, the system simultaneously provides the heated sCO_2 and air flows at various flow rates. All measured data are post-processed by a data acquisition setup consisting of voltage input modules obtaining temperature and pressure signals, a module chassis, and a laptop with a custom data reading and storage program. Steady-state data, which is the average value of 600 signals in 10 minutes after all temperatures and pressures are stable, for each measurement are collected and saved by this system. Detailed information on specific instruments is provided in section 2.3.

2.2. Fabricated MT-STHX

The MT-STHX consists of a staggered tube bundle with 39 microtubes (inner diameter = 1.75mm) over 13 rows and 6 columns, as shown in Figure 2a. The internal (tube-side) flow is sCO_2 (up to 200 ^oC and 100 bar) and the external (shell-side) flow is pressurized air (up to 3 bar and 300 ^oC). Stainless Steel 304 was selected as the HX material because it has very similar thermal conductivity to many high-temperature alloys for sCO_2 containment, such as Inconel 625, 718, and Haynes 282. The HX geometry imitates half of the geometry of a standardized U-tube configuration (namely CFU

configuration) from TEMA [35]. On both sides of the tube bundle, half-round sealing strips are utilized to minimize flow bypass effects [44,45].

Figure 2b and c contain exploded views of the HX assembly and present the main components within this sCO_2-air HX. The microtubes are arc-welded from the two tube sheets and form the tube bundle section of the STHX. Four segmenting baffles are evenly distributed in the tube bundle region to provide five flow passes for the external flow. The front (curved) and back (straight) shells with sealing strip structures [44,45] are designed to maintain the shape of cross-section. Flange plates and inlet and outlet tubes are welded to shells and tube sheets. High-temperature graphite and rubber gaskets are used to seal the mating surfaces, with high-temperature metal sealant, bolts, nuts, and washers. Multiple instrumentation tubes are available to measure temperature and pressure at the inlet, outlet, and local positions within the HX. Swagelok® compression fittings are used to connect the HX with the integrated test system and necessary instruments. Multiple hydrostatic pressure tests up to 110 bar were completed for the tube bundle section to prove that the tube side of the HX can withstand high pressure sCO_2 flow without leakage. Insulation blankets made of ceramic fibers are wrapped around the HX to minimize heat loss during experiments. Critical design details are shown in Figure 3 and Table 1, respectively.

Table 1. Critical design parameters for the MT-STHX

Parameters	Current MT-STHX	TEMA Standards for Conventional STHXs [35]	Design Consideration
Tube ID, D_{it} [mm]	1.75	> 4.9	The selected tube is a microtube
Tube wall thickness, δ_t [mm]	0.71	> 0.4	The selected wall thickness is > 33% of the tube ID to provide sufficient creep and fatigue resistance for extreme conditions in commercial sCO_2 MT-STHXs
Longitudinal pitch/tube OD, P_l/D_{ot}	1.50	> 1.25	All selected pitch ratios follow the TEMA standards [35] and are close to limit values for fabricating the tube sheets in commercial sCO_2 MT-STHXs
Transverse pitch/tube OD, P_t/D_{ot}	2.65	> 1.25	
Diagonal pitch/tube OD, P_d/D_{ot}	1.52	> 1.25	
Number of tube rows, N_{tr}	13	> 12	The selected numbers of tube rows and columns are sufficiently large to be representative and minimize the HX shell ID
Number of tube columns, N_{tc}	6	> 3	
Baffle spacing to shell ID ratio	0.67	0.2-1.0	The selected baffle spacing follows the TEMA standard and enables a large external Reynolds number ranging from 1,500 to 12,000
Baffle cut to tube diameter ratio	0.25	0.15-0.45	The selected baffle cut follows the TEMA standard and a moderate value is selected
Shell ID, D_{is} [mm]	70.1	-	The selected shell ID is the minimum value to accommodate the tube bundle
Shell (tube) length, L_s [mm]	228.6	-	The shell (tube) length is 5 times the baffle spacing because the HX has 5 flow paths

2.3. Instrumentation

Figure 4a indicates the instrumentation locations and all measured parameters for internal (sCO_2) and external (air) flows during the thermohydraulic tests. The mass flow rates for internal flow ($\dot{m}_i$) and external flow ($\dot{m}_e$) are measured by flow meters or mass flow controllers before they enter the HX. Four thermocouple probes and pressure transducers are installed with Swagelok® compression fittings to measure the inlet and outlet temperatures (T_{ii}, T_{io}, T_{ei}, and T_{eo}) and pressures (P_{ii}, P_{io}, P_{ei}, and P_{eo}), at inlet and outlet ports (2.54 cm away from the entrance and exits on both flow sides). The thermocouple probes are K-type, with outer diameter of 1.59 mm (1/16 inches). Multiple pressure transducers measure the static pressure of high-temperature flow with ±1% accuracy. Both instruments are calibrated by vendors, following the National Institute of Standards and Technology (NIST) standards. In addition, local temperatures and pressures in the external flow are measured through the instrumentation tubes on the back shell. Measured data for four locations, L_1 to L_4, are reported here because they are the inlets and outlets for the 2nd, 3rd, and 4th unit cells. All thermocouple probe tips are located at the center of mass in the flow cross-sections as shown in Figure 4b. During an additional hydraulic test (no heat input), manometers were used to measure pressure drops in 1st to 5th unit cells (between the external inlet and L1, L1 and L2, …, L4 and the external outlet) at turns. In comparison to the pressure transducer measurement, the manometers directly measure the pressure difference and provide higher accuracy (the accuracy of the manometer and pressure transducers used in this work are ±0.5% and ±1%, respectively).

3. DATA REDUCTION AND ERROR ANALYSIS

The tube inner diameter, D_{it}, and tube bundle hydraulic diameter, D_h, are typically used as characteristic lengths for internal and external flow, respectively. According to Kays and London [46], the hydraulic diameter is defined as:

$$D_h = \frac{4A_c X_l}{A_{HT}} \tag{1}$$

where A_c is the minimum flow cross-sectional area, X_l is the flow length (longitudinal pitch × number of tube rows), and A_{HT} is the total heat transfer area for the external flow. All three parameters are constant for a given STHX geometry. Based on these characteristic lengths, the Reynolds numbers for internal and external flows are:

$$Re_i = \frac{\rho_{avg} u_{i,avg} D_{it}}{\mu_{i,avg}} = \frac{4\dot{m}_i}{\pi N_t D_{it} \mu_{i,avg}} \quad (2)$$

$$Re_e = \frac{\rho_{avg} u_{e,max} D_h}{\mu_{e,avg}} = \frac{4\dot{m}_e X_l}{A_{HT} \mu_{e,avg}} \quad (3)$$

where $\mu_{i,avg}$ and $\mu_{e,avg}$ are average viscosities of the internal and external flow, respectively.

Utilizing temperature and pressure measurements, flow enthalpies (h) are obtained from the CoolProp database [47] to calculate internal thermal power, Q_i, the external power, Q_e, and the ideal HX power, Q_{ideal} as shown below:

$$Q_i = \dot{m}_i [h_{io}(T_{io}, P_{io}) - h_{ii}(T_{ii}, P_{ii})] \quad (4)$$

$$Q_e = \dot{m}_e [h_{ei}(T_{ei}, P_{ei}) - h_{eo}(T_{eo}, P_{eo})] \quad (5)$$

$$Q_{ideal} = min\{\dot{m}_e [h_{ei}(T_{ei}, P_{ei}) - h_{eo,min}(T_{ii}, P_{eo})],\ \dot{m}_i [h_{io,max}(T_{ei}, P_{io}) - h_{ii}(T_{ii}, P_{ii})]\} \quad (6)$$

For the MT-STHX, Q_i theoretically equals to the HX power (namely HX capacity), while Q_e is the sum of the HX power and heat loss through the insulation. Therefore, HX effectiveness is derived as:

$$\varepsilon = \frac{Q_i}{Q_{ideal}} \quad (7)$$

The HX thermal conductance, UA, is calculated using the power and log-mean temperature difference:

$$UA = \frac{Q_i}{\Delta T_{lm}} \quad (8)$$

$$\Delta T_{lm} = \frac{(T_{io} - T_{ei}) - (T_{ii} - T_{eo})}{\ln \frac{T_{io} - T_{ei}}{T_{ii} - T_{eo}}} \quad (9)$$

Pressure drops and HX power are important performance metrics and are calculated from temperature and pressure data. The total external pressure drop, ΔP_{tot}, and single unit cell (1st to 5th unit cell) pressure drops, ΔP_k $(k = 1, 2, \ldots 5)$, are used to quantify flow friction in the fabricated STHX, as defined by:

$$\Delta P_{tot} = P_{ei} - P_{eo} \tag{10}$$

$$\Delta P_1 = P_{ei} - P_{L1} \tag{11}$$

$$\Delta P_k (k = 2,3,4) = P_{Lk} - P_{Lk-1} \tag{12}$$

$$\Delta P_5 = P_{L4} - P_{eo} \tag{13}$$

Local pressure drop data on the shell-side are used to estimate the tube bundle pressure drop $\Delta P_{tb,k}$ and the average friction factor f_k for the k[th] unit cell (valid for k=2, 3, and 4) [46] for flow over the tube bundle:

$$\Delta P_{tb,k} = \Delta P_k - \Delta P_{uw,k} - \Delta P_{lw,k} \tag{14}$$

$$f_k = \frac{\Delta P_{tb,k}}{\frac{1}{2}\rho_{k,avg} u_{max,k}^2 \frac{4X_l}{D_h}} \tag{15}$$

In these equations, $\Delta P_{tb,k}$ is the overall pressure drop of the k[th] unit cell less the pressure drops in the upper window regions ($\Delta P_{uw,k}$) and bottom ($\Delta P_{lw,k}$) of the tube bundle. These window region pressure drops are calculated from ref. [34]:

$$\Delta P_{uw,k} = \frac{\dot{m}_e^2}{\rho_{Lk-1} A_s A_w} \tag{16}$$

$$\Delta P_{lw,k} = \frac{\dot{m}_e^2}{\rho_{Lk} A_s A_w} \tag{17}$$

where A_s is the interspace front plane area through the tube bundle and A_w is the cross-sectional area of the window inlet/outlet. ρ_{Lk-1} and ρ_{Lk} are the densities of external flow at the locations Lk-1 and Lk (k=2,3, and 4), respectively, as shown in Figure 4. They are obtained from the CoolProp database [47] using measured temperatures and pressures at these locations.

As discussed in section 2.1, the collected data in this study are the average values of the 600 signals after they reach steady state. Therefore, the dataset has very low precision uncertainty, and experimental uncertainty primarily derives from bias errors caused by device inaccuracies. The propagated errors of calculated parameters such as HX power are estimated from [48]:

$$\frac{\delta y}{y} = \pm \sqrt{\sum_{i=1}^{n} \left(\frac{\partial y}{\partial x_i} \frac{\delta x_i}{y} \right)^2} \times 100\% \quad (18)$$

where $y = f(x_1, x_2, \ldots, x_n)$ represents any calculated performance parameter and is a function of $x_1, x_2, \ldots, x_n$, which are measured parameters. For example, the sCO_2-side (internal) power, Q_i, is proportional to the internal flow rate, $\dot{m}_i$, and the enthalpy difference between the flow inlet and outlet, $(h_{io} - h_{ii})$, which is predominantly a function of measured temperatures. The experimental error for Q_i can be expressed as $\frac{\delta Q_i}{Q_i} = \pm\sqrt{\left(\frac{\delta \dot{m}_i}{\dot{m}_i}\right)^2 + \left(\frac{\delta T_{io}}{T_{io}}\right)^2 + \left(\frac{\delta T_{ii}}{T_{ii}}\right)^2}$ based on Equation 18. The errors for the other metrics are calculated in a similar way. All relevant experimental errors are listed in Table 2.

Table 2. Bias errors of measured parameters and calculated performance metrics

Measured Parameters		**Calculated Performance Metrics**	
Parameter	**Error**	**Parameter**	**Error**
Temperature [K]	$\frac{\delta T}{T} = \pm 0.75\%$	sCO_2-side power [W]	$\frac{\delta Q_i}{Q_i} = \pm 1.2\%$
sCO_2 pressure [MPa]	$\frac{\delta P_i}{P_i} = \pm 1.0\%$	Air-side power [W]	$\frac{\delta Q_e}{Q_e} = \pm 1.3\%$
sCO_2 mass flow rate [kg/s]	$\frac{\delta \dot{m}_i}{\dot{m}_i} = \pm 0.50\%$	HX effectiveness	$\frac{\delta \varepsilon}{\varepsilon} = \pm 1.8\%$
Air pressure [kPa]	$\frac{\delta P_e}{P_e} = \pm 1.0\%$	ΔT_{lm} [°C]	$\frac{\delta \Delta T_{lm}}{\Delta T_{lm}} = \pm 2.1\%$
Air pressure drop (by manometer) [kPa]	$\frac{\delta \Delta P_e}{\Delta P_e} = \pm 0.50\%$	UA [W/K]	$\frac{\delta UA}{UA} = \pm 2.3\%$
Air mass flow rate [kg/s]	$\frac{\delta \dot{m}_e}{\dot{m}_e} = \pm 0.75\%$	Air-side friction factor	$\frac{\delta f}{f} = \pm 1.2\%$

4. RESULTS & DISCUSSION

Multiple experiments were completed with the MT-STHX test system, and steady-state data were recorded. Critical HX performance metrics were calculated and compared with numerical predictions from the model of Krishna et al. [42,43].

4.1 Thermohydraulic tests

Thirty-six experimental cases with varying rates of external (air) and internal (sCO_2) flows were performed for the MT-STHX. Nine air flow rates (5, 10, …, 45 g/s) and four sCO_2 flow rates (12, 15, 18, and 21 g/s) were selected. In each case, the air flow inlet temperature was influenced by the air heater capacity and therefore varied from 166 to 108 °C with increasing flow rate. Given that the air flow loop was open, the air inlet pressure was dominated by the external pressure drops of STHX and air cooler. The inlet conditions for sCO_2 flow were controlled by the sCO_2 loop system with the inlet pressure at around 100 bar. The inlet temperature was set to be 70 or 60 °C to maintain the supercritical state and to provide sufficient temperature difference between two flow streams. The full data sets are shown in ref. [51].

Figure 5 shows the thermal power comparison between internal and external streams for all 36 test cases. The results indicate that the power deviation between the sCO_2 and air sides falls within ± 10% (average deviation = 4.4%) and implies that all tests reached steady state with an acceptable heat balance. Most cases have slightly higher air flow power because the air flow is on the external side and encounters a small environmental heat loss.

Variations of critical performance metrics are plotted in Figure 6 as functions of external Reynolds number. Figure 6a shows the heat exchanger capacity from thirty-six thermohydraulic tests. The capacity increases with Re_e from 1000 to 8000 because the air heat transfer rate increases, and the inlet temperatures (or heater outlet temperature) are maintained above 150 °C. When Re_e > 8000, the air heater reaches full power, and its temperature output cannot be maintained with increasing Reynolds number. Therefore, the set temperature of the air heater outlet is reduced to protect the heater from overloading, causing significant drops and complex variations for the HX inlet temperature and capacity.

Figure 6b shows heat exchanger effectiveness and indicates the selected flow rates cover a wide effectiveness range. At low Re_e, ε is relatively high because the external flow outlet temperature is similar to the internal flow inlet temperature. In this scenario, ideal HX power, Q_{ideal}, is calculated

based on the external flow and is very close to the actual HX power, Q_i. With Re_e increasing from 0 to 5000, both Q_{ideal} and Q_i rise while Q_{ideal} has a higher increment, which results in a reduction of ε. On the other hand, when Re_e becomes sufficiently large, Q_{ideal} is calculated from the internal flow, reversing the trend of Q_{ideal} and ε. Effectiveness first increases and then decreases with increasing Re_e in most cases. When the internal flow rate is relatively high, this trend is not apparent because ε is also affected by the heater outlet temperature, which decreases with Re_e for $Re_e >$ 8000.

The variation of the HX conductance UA and the relevant trend lines are presented in Figure 6c. UA increases with both internal and external flow rates with a power-law Reynolds number dependence. The total air flow pressure drop on the external side increases linearly with external Reynolds number, as shown in Figure 6d. Data for various internal flow rates fall on top of each other because variations in internal flow rate at a given external flow rate affects only the external flow temperature profile and air properties, which have negligible effects on external pressure drops. The total external pressure drop is relatively complex and consists of contributions from all unit cells. In each unit cell, pressure drop occurs in both the tube bundle and window regions. To better understand the characteristics of pressure drops on the external side of the MT-STHX, additional tests with no heat input were performed and are described in the next section.

4.2 Additional hydraulic tests

Given that the temperature and property variations do not significantly affect the pressure drop trend, additional hydraulic tests for external flow were performed without any heat input. Temperatures and pressures at inlet and outlet planes of each unit cell are measured in sequence to obtain density and viscosity data for Reynolds number calculations. High-accuracy manometers were utilized to measure pressure drops in each unit cell to achieve less bias error. The measured data are shown in ref. [51].

Figure 7a compares the external pressure drop of each unit cell for Reynolds number ranging from 2000 to 18000. Unit cell pressure drops increase in sequence because the flow density decreases and velocity increases along the flow path. However, the pressure drop in the 5th unit cell is much larger than other cells, indicating that the external flow outlet port causes additional pressure drop due to sudden contraction of the flow cross-sectional area when flow exits the last unit cell. In addition, the pressure drop in the 1st unit cell is also affected by the entrance port and is significantly lower than

other cells. Both entrance and exit effects can be different for various wrap configurations of HXs and therefore are not further considered in this study. Pressure drops of all cells, the central three cells, and the 3rd unit cell are plotted together in Figure 7b. The total pressure drop is significantly higher than five times the 3rd unit cell pressure drop, which is mainly caused by flow exit effects. When neglecting the 1st and the 5th unit cells, the pressure drop of the central three cells is very close to 3 times the 3rd unit cell pressure drop. This observation implies that the central three cells encounter much less effect of the exit and entrance and are relatively more representative.

Figure 8a and b compare the tube bundle pressure drops and average friction factors of the central three cells, calculated by Equation (14) and (15), respectively. The deviations between 2nd and 3rd unit cells for both parameters are small and mainly caused by the difference in density of air. However, the 4th unit cell has a significantly higher tube bundle pressure drop and friction factor compared to the 2nd and 3rd unit cells, indicating that the exit effect might significantly affect the hydraulic behavior in the 4th unit cell. Therefore, this study uses pressure drops from the 2nd and 3rd unit cells as representative data for further analysis. Their hydraulic behaviors are expected to be similar to most unit cells in a commercial MT-STHX with a large number of unit cells.

4.3 Comparison with model predictions

The experimental results are compared with model predictions to provide further validation of the model from Krishna et al. [42, 43], which is a 2D numerical model for sCO_2 STHXs. The governing equations in this model are conservation equations based on the concept of volume averaging. Empirical correlations are utilized to achieve closure of the governing equations. The internal correlations for the Nusselt number and the friction factor are from Petukhov [49] and Gnienski [50], respectively, and the external correlations were originally developed as follows:

$$j_H = 0.41\left(\frac{D_h}{D_E}\right)^{0.50}\left(\frac{P_t}{D_{ot}}\right)^{-0.18}\left(\frac{P_l}{D_{ot}}\right)^{-0.16}\mathrm{Re}_{D_h}^{-0.38} \tag{19}$$

$$f = 0.63\left(\frac{D_h}{D_{ot}}\right)^{0.89}\left(\frac{P_t}{D_{ot}}\right)^{-0.09}\left(\frac{P_l}{D_{ot}}\right)^{-0.53}\mathrm{Re}_{D_h}^{-0.21} \tag{20}$$

Bell-Delaware correction factors [33, 34] are used to compensate for flow leakage between tubes and baffles and between baffles and the shell. These correlations and correction factors agreed well with CFD results in Krishna et al. [42, 43], while the current experimental study provides a more comprehensive validation for the whole model. To obtain the model predictions for all tested cases,

the inlet flow rates, temperatures, and pressures of both streams in the experiments are input to the model, and relevant HX performance metrics are calculated as model outputs.

Figure 9a illustrates a comparison of HX effectiveness obtained from experimental results and model predictions. The maximum and average deviations (absolute difference) for all 36 cases are 6.1% and 2.1%, respectively. All compared cases have deviations within ±10%, indicating that the model accurately predicts the effectiveness of this STHX. The overall heat transfer coefficients (defined in Equation 8) from experiments and model predictions are plotted in Figure 9b. The maximum and average deviations for all 36 cases are 12% and 6.6%, respectively. In total, thirty-four cases exhibit good agreement with model predictions within 10% deviation.

These results in this section provide a thorough validation of this numerical model to predict heat transfer performance of MT-STHXs with different working fluids. All predictions slightly underestimate the heat transfer coefficients in the HX, and the mismatch increases with the increasing internal Reynolds number. The primary cause is that the model does not account for heat loss from the external flow and predicts higher ΔT_{lm} (inversely proportional to heat transfer coefficient) than the experimental results. In future scaled-up MT-STHXs with less heat loss, the temperature difference between the two streams may be larger, and the model agreement is expected to improve even further.

Comparison data for total external pressure drop obtained from the thermohydraulic and additional hydraulic experiments are plotted in Figure 10a and b. The maximum and average deviations between the experimental and model results for both datasets are 13% and 8.0%, respectively. To avoid the entrance and exit effects in the first and last unit-cells, Figure 10c compares the pressure drop between the 2nd and 4th unit cells in the additional hydraulic tests with the model predictions. The maximum and average deviations are found to be 8.2% and 3.3% respectively, which is much less than the deviation for the total external pressure drop. In addition, the pressure drop comparison for the representative (3rd) unit cell shows an even closer agreement (4.3% for the maximum deviation and 1.4% for the average), as shown in Figure 10d. This finding shows that the model can accurately predict the pressure drop for the representative unit cell in this study and should have sufficient accuracy for estimating the hydraulic performance of industrial-scale MT-STHXs, in which most unit cells will behave in a representative manner without exit or entrance effects. More detailed calculation and comparisons have been conducted for the representative (2nd and 3rd) unit cells in this study. Figure 11a and b show average friction factors of tube bundles in the

2nd and 3rd unit cells from the experiments and model predictions. Deviations for all cases are within ±10%, and the average deviation is 3.1%, indicating that the developed friction factor correlation (Equation 20) in the model is highly accurate, and the method used to calculate the pressure drops in window and tube bundle regions is appropriate.

A sensitivity analysis was performed to assess the effects of inlet parameters on the deviations between the experimental and modeling results. Figure 12a and b plot the UA of the HX as a function of air (external) Reynolds numbers and sCO_2 (internal) Reynolds number, respectively. When both Reynolds numbers are low, the two results agree well. At high Reynolds numbers, especially for internal flow, the deviations become more significant. This outcome is likely caused by the increased complexity of property variations and flow regimes for sCO_2 at higher Reynolds numbers. In Figure 12c, the results indicate that model predictions of total external pressure drop deviate more as external Reynolds number increases. This trend might be caused by entrance and exit effects that are more prominent at higher Reynolds numbers. For the part of the HX that is less affected by these effects, such as the central unit cell, the deviation of the external pressure drop becomes negligible, as shown in Figure 12d. While the friction factor prediction seems to be less accurate when Reynolds number is smaller than 5000 or larger than 15000, the largest deviation observed in this study is still less than 5%. Therefore, the current analysis qualitatively and quantitively confirms the validity of the selected model and correlations and provides high confidence for using these tools in future design and optimization studies of MT-STHXs.

5. CONCLUSIONS

A five-unit-cell MT-STHX has been fabricated, and an integrated experimental system with sCO_2 and air as working fluids is reported. Multiple sets of thermohydraulic experiments on the fabricated MT-STHX are performed and reported over an extensive range of tube-side and shell-side Reynolds numbers. Experimental results are compared with predictions from a previously published 2D numerical model. Major conclusions include:

1. The fabricated MT-STHX contains representative design features for the same type of sCO_2 HXs at commercial scales and provides a basis for design and fabrication.
2. The performed experiments provide thermohydraulic performance datasets for MT-STHXs with sCO_2 and air as working fluid. The sCO_2 Reynolds number varies from 9,000 to 17,000, and the air Reynolds number ranges from 2,000 to 18,000.

3. The 1st, 4th, and 5th unit cells in the fabricated MT-STHX have non-negligible entrance and exit effects at high Reynolds numbers. Conversely, the 2nd and 3rd cells exhibit similar performance characteristics and can be considered representative unit cells that have similar behavior to cells in scaled-up MT-STHXs.
4. Experimental results in this paper provide a thorough validation of the correlations and the 2D numerical model from Krishna et al. [42,43] to predict the thermohydraulic performance of a sCO_2 MT-STHX.

The sCO_2 MT-STHX is a promising configuration for sCO_2 heat exchangers that is still in early stages of development. Future studies should focus on heat exchanger design and optimization for enhanced thermohydraulic performance and increased power densities. Advancements in material stability and manufacturing methods will also be needed to scale this HX technology to the industrial level for future high-performance sCO_2 power cycles.

Acknowledgment

The authors thank ARPA-E and UCLA for their funding and Dr. Nasr Ghoniem, Dr. Xiaochun Li, and Honeywell Aerospace for their research collaboration and insightful feedback.

FUNDING

The information, data, or work presented herein was funded in part by the Advanced Research Projects Agency-Energy (ARPA-E), US Dept. of Energy, under Award Number DE-AR0001131, in collaboration with Honeywell Aerospace. The information, data, or work presented herein was funded in part by an agency of the United States Government. Neither the United States Government nor any agency thereof, nor any of their employees, makes any warranty, express or implied, or assumes any legal liability or responsibility for the accuracy, completeness, or usefulness of any information, apparatus, product, or process disclosed, or represents that its use would not infringe privately owned rights. Reference herein to any specific commercial product, process, or service by trade name, trademark, manufacturer, or otherwise does not necessarily constitute or imply its endorsement, recommendation, or favoring by the United States Government or any agency thereof. The views and opinions of authors expressed herein do not necessarily state or reflect those of the United States Government or any agency thereof.

Nomenclature

A_c	shell-side minimum cross-sectional area [m^2]
A_{HT}	heat transfer area [m^2]
A_s	shell-side interspace area [m^2]
A_w	shell-side window region cross-sectional area [m^2]
D_h	hydraulic diameter [m]
D_{it}	tub inner diameter [m]
D_{ot}	tube outer diameter [m]
D_{is}	shell inner diameter [m]
f	friction factor
h	specific enthalpy [J/kg]

L	instrumentation location within the HX
L_s	shell length [m]
$\dot{m}$	mass flow rate [kg/s]
N_{tr}	number of tube rows
N_{tc}	number of tube columns
P	pressure [Pa]
P_d	tube diagonal pitch [m]
P_l	tube longitudinal pitch [m]
P_t	tube transverse pitch [m]
Q	thermal power [W]
Re	Reynolds number
T	temperature [^{o}C]
U	overall heat transfer coefficient [W/m^2·K]
u	flow velocity [m/s]
x	measured parameter
X_l	shell-side flow length
y	calculated parameter

Greek Symbols

δ	thickness [m]
μ	viscosity [Pa·s]
ρ	density [kg/m^3]
ε	heat exchanger effectiveness

Subscript

avg	average
e	external flow
ei	external flow inlet
eo	external flow outlet

exp	experiments
i	internal flow
ii	internal flow inlet
io	internal flow outlet
lm	log-mean
max	maximum
min	minimum
tot	total

Acronyms

CFD	computational fluid dynamics
CSP	concentrated solar power
sCO_2	supercritical carbon dioxide
HX	heat exchanger
ID	inner diameter
LMTD	log-mean temperature difference
OD	outer diameter
PCHX	printed circuit heat exchanger
STHX	shell-and-tube heat exchanger
WHP	waste heat to power

REFERENCE

1. Feher, E. G. (1968). The supercritical thermodynamic power cycle. *Energy conversion*, 8(2), 85-90.
2. Ahn, Y., Bae, S. J., Kim, M., Cho, S. K., Baik, S., Lee, J. I., & Cha, J. E. (2015). Review of supercritical CO2 power cycle technology and current status of research and development. *Nuclear engineering and technology*, 47(6), 647-661.
3. Yamaguchi, H., Sawada, N., Suzuki, H., Ueda, H., & Zhang, X. R. (2010). Preliminary study on a solar water heater using supercritical carbon dioxide as working fluid. *Journal of Solar Energy Engineering*, 132(1).

4. Persichilli, M., Kacludis, A., Zdankiewicz, E., & Held, T. (2012). Supercritical CO2 power cycle developments and commercialization: why sCO2 can displace steam. *Power-Gen India & Central Asia*, 2012, 19-21.
5. Miller, J. D., Buckmaster, D. J., Hart, K., Held, T. J., Thimsen, D., Maxson, A., ... & Hume, S. (2017, June). Comparison of supercritical CO2 power cycles to steam Rankine cycles in coal-fired applications. In *Turbo Expo: Power for Land, Sea, and Air* (Vol. 50961, p. V009T38A026). American Society of Mechanical Engineers.
6. Pérez-Pichel, G. D., Linares, J. I., Herranz, L. E., & Moratilla, B. Y. (2012). Thermal analysis of supercritical CO2 power cycles: Assessment of their suitability to the forthcoming sodium fast reactors. *Nuclear Engineering and Design*, 250, 23-34.
7. Guo, Z., Zhao, Y., Zhu, Y., Niu, F., & Lu, D. (2018). Optimal design of supercritical CO2 power cycle for next generation nuclear power conversion systems. *Progress in Nuclear Energy*, 108, 111-121.
8. Alsagri, A. S., Chiasson, A., & Gadalla, M. (2019). Viability assessment of a concentrated solar power tower with a supercritical CO2 Brayton cycle power plant. *Journal of Solar Energy Engineering*, 141(5).
9. Guelpa, E., & Verda, V. (2020). Exergoeconomic analysis for the design improvement of supercritical CO2 cycle in concentrated solar plant. *Energy*, 206, 118024.
10. Wang, X., & Dai, Y. (2016). Exergoeconomic analysis of utilizing the transcritical CO2 cycle and the ORC for a recompression supercritical CO2 cycle waste heat recovery: A comparative study. *Applied energy*, 170, 193-207.
11. Song, J., Li, X. S., Ren, X. D., & Gu, C. W. (2018). Performance improvement of a preheating supercritical CO2 (S-CO2) cycle based system for engine waste heat recovery. *Energy Conversion and Management*, 161, 225-233.
12. Son, S., Heo, J. Y., & Lee, J. I. (2018). Prediction of inner pinch for supercritical CO2 heat exchanger using Artificial Neural Network and evaluation of its impact on cycle design. *Energy conversion and management*, 163, 66-73.
13. Yoo, B., Kulak, R. F., & Kim, Y. J. (2006, January). Pressure and thermal stress analyses of a generation IV reactor system, mini-channel heat exchanger. In *International Conference on Nuclear Engineering* (Vol. 42444, pp. 167-171).

14. Utamura, M. (2007, January). Thermal-hydraulic characteristics of microchannel heat exchanger and its application to solar gas turbines. In *Turbo Expo: Power for Land, Sea, and Air* (Vol. 47934, pp. 287-294).
15. Liu, G., Huang, Y., Wang, J., & Liu, R. (2020). A review on the thermal-hydraulic performance and optimization of printed circuit heat exchangers for supercritical CO2 in advanced nuclear power systems. *Renewable and Sustainable Energy Reviews*, 133, 110290.
16. Li, Q., Flamant, G., Yuan, X., Neveu, P., & Luo, L. (2011). Compact heat exchangers: A review and future applications for a new generation of high temperature solar receivers. *Renewable and Sustainable Energy Reviews*, 15(9), 4855-4875.
17. Kwon, J. S., Son, S., Heo, J. Y., & Lee, J. I. (2020). Compact heat exchangers for supercritical CO2 power cycle application. *Energy Conversion and Management*, 209, 112666.
18. Meshram, A., Jaiswal, A. K., Khivsara, S. D., Ortega, J. D., Ho, C., Bapat, R., & Dutta, P. (2016). Modeling and analysis of a printed circuit heat exchanger for supercritical CO2 power cycle applications. *Applied Thermal Engineering*, 109, 861-870.
19. Ren, Z., Zhang, L., Zhao, C. R., Jiang, P. X., & Bo, H. L. (2021). Local Flow and Heat Transfer of Supercritical CO2 in Semicircular Zigzag Channels of Printed Circuit Heat Exchanger during Cooling. *Heat Transfer Engineering*, 42(22), 1889-1913.
20. Saeed, M., & Kim, M. H. (2017). Thermal and hydraulic performance of SCO2 PCHE with different fin configurations. *Applied thermal engineering*, 127, 975-985.
21. Li, X. L., Tang, G. H., Fan, Y. H., Yang, D. L., & Wang, S. Q. (2019). Numerical analysis of slotted airfoil fins for printed circuit heat exchanger in S-CO2 Brayton Cycle. *Journal of Nuclear Engineering and Radiation Science*, 5(4).
22. Wen, Z. X., Lv, Y. G., Li, Q., & Zhou, P. (2020). Numerical study on heat transfer behavior of wavy channel supercritical CO2 printed circuit heat exchangers with different amplitude and wavelength parameters. *International Journal of Heat and Mass Transfer*, 147, 118922.
23. Khoshvaght-Aliabadi, M., Ghodrati, P., Mortazavi, H., & Kang, Y. T. (2022). Predicting heat transfer and flow features of supercritical CO2 in printed circuit heat exchangers with novel wavy minichannels. *International Journal of Heat and Mass Transfer*, 196, 123232.
24. Cheng, K., Zhou, J., Zhang, H., Huai, X., & Guo, J. (2020). Experimental investigation of thermal-hydraulic characteristics of a printed circuit heat exchanger used as a pre-cooler for the supercritical CO2 Brayton cycle. *Applied Thermal Engineering*, 171, 115116.

25. Park, J. H., Kwon, J. G., Kim, T. H., Kim, M. H., Cha, J. E., & Jo, H. (2020). Experimental study of a straight channel printed circuit heat exchanger on supercritical CO2 near the critical point with water cooling. *International Journal of Heat and Mass Transfer*, 150, 119364.
26. Chu, W., Li, X., Chen, Y., Wang, Q., & Ma, T. (2021). Experimental study on small scale printed circuit heat exchanger with zigzag channels. *Heat Transfer Engineering*, 42(9), 723-735.
27. Chang, H., Han, Z., Li, X., Ma, T., & Wang, Q. (2022). Experimental study on heat transfer performance of sCO2 near pseudo‐critical point in airfoil‐fin PCHE from viewpoint of average thermal‐resistance ratio. *International Journal of Heat and Mass Transfer*, 196, 123257.
28. Zhang, X., Keramati, H., Arie, M., Singer, F., Tiwari, R., Shooshtari, A., & Ohadi, M. (2018). Recent developments in high temperature heat exchangers: A review. *Frontiers in Heat and Mass Transfer (FHMT)*, 11, 18
29. Chordia, L., Portnoff, M. A., & Green, E. (2017). *High temperature heat exchanger design and fabrication for systems with large pressure differentials* (No. DE-FE0024012). Thar Energy, LLC, Pittsburgh, PA (United States).
30. Moisseytsev, A., Lv, Q., & Sienicki, J. J. (2017, June). Heat Exchanger Options for Dry Air Cooling for the sCO2 Brayton Cycle. In *Turbo Expo: Power for Land, Sea, and Air* (Vol. 50961, p. V009T38A006). American Society of Mechanical Engineers.
31. Marion, J., Lariviere, B., McClung, A., & Mortzheim, J. (2021, June). The STEP 10 MWe sCO2 Pilot Demonstration Status Update. In *Turbo Expo: Power for Land, Sea, and Air* (Vol. 85048, p. V010T30A011). American Society of Mechanical Engineers.
32. Li, W., Yu, Z., Wang, Y., & Li, Y. (2022). Heat transfer of supercritical carbon dioxide in a tube-in-tube heat exchanger-a CFD study. *The Journal of Supercritical Fluids*, 181, 105493.
33. Shah, R. K., & Sekulic, D. P. (2003). *Fundamentals of heat exchanger design*. John Wiley & Sons.
34. Thulukkanam, K. (2000). *Heat exchanger design handbook*. CRC press.
35. TEMA (2019), *Standards of the tubular exchanger manufacturers association*, 10th ed. Tubular Exchanger Manufacturers Association, New York.
36. Jiang, Y., Liese, E., Zitney, S. E., & Bhattacharyya, D. (2018). Optimal design of microtube recuperators for an indirect supercritical carbon dioxide recompression closed Brayton cycle. *Applied energy*, 216, 634-648.
37. Chai, L., & Tassou, S. A. (2022). Modeling and Evaluation of the Thermohydraulic Performance of Compact Recuperative Heat Exchangers in Supercritical Carbon Dioxide Waste Heat to Power Conversion Systems. *Heat Transfer Engineering*, 43(13), 1067-1082.

38. Chai, L., & Tassou, S. A. (2022). Performance analysis of heat exchangers and integrated CO2 supercritical Brayton cycle for varying heat carrier, cooling and working fluid flow rates. *Heat Transfer Engineering*, 1(21), 0145-7632.
39. Cai, H. F., Liang, S. Q., Guo, C. H., Wang, T., Zhu, Y. M., & Jiang, Y. Y. (2020). Numerical investigation on heat transfer of supercritical carbon dioxide in the microtube heat exchanger at low Reynolds numbers. *International Journal of Heat and Mass Transfer*, 151, 119448.
40. Cai, H. F., Jiang, Y. Y., Wang, T., Liang, S. Q., & Zhu, Y. M. (2020). Experimental investigation on convective heat transfer and pressure drop of supercritical CO2 and water in microtube heat exchangers. *International Journal of Heat and Mass Transfer*, 163, 120443.
41. Krishna, A. B., Jin, K., and & Fisher, T. S. Modeling for supercritical CO2 shell-and-tube heat exchangers under extreme conditions. Part 1: Correlation development. *Journal of Heat Transfer*
42. Krishna, A. B., Jin, K., and & Fisher, T. S. Modeling for supercritical CO2 shell-and-tube heat exchangers under extreme conditions. Part 2: Heat exchanger model. *Journal of Heat Transfer*
43. Krishna, A. B., Jin, K., Ayyaswamy, P. S., Catton, I., & Fisher, T. S. (2022). Technoeconomic optimization of superalloy supercritical CO2 microtube shell-and-tube-heat exchangers. Applied Thermal Engineering, 119578.
44. Taylor, C. E., & Currie, I. G. (1987). Sealing strips in tubular heat exchangers. *Journal of Heat Transfer*, 109, 569-574
45. Martin, D. J., Hollingworth, M. A., Mayhew, V. R., & Haseler, L. E. (1989). *The effect of bypass lanes and sealing-strips in shell-and-tube heat exchangers* (Doctoral dissertation, University of Bristol).
46. Kays, W. M., & London, A. L. (1984). Compact heat exchangers. McGraw-Hill Book Company
47. Bell, I. H., Wronski, J., Quoilin, S., & Lemort, V. (2014). Pure and pseudo-pure fluid thermophysical property evaluation and the open-source thermophysical property library CoolProp. *Industrial & engineering chemistry research*, 53(6), 2498-2508.
48. Jcgm, J. C. G. M. (2008). Evaluation of measurement data—Guide to the expression of uncertainty in measurement. *Int. Organ. Stand. Geneva ISBN*, 50, 134.
49. Petukhov, B. S. (1970). Heat transfer and friction in turbulent pipe flow with variable physical properties. *Advances in heat transfer*, Vol. 6, 503-564.
50. Gnielinski, V. (1975). New equations for heat and mass transfer in the turbulent flow in pipes and channels. *NASA STI/recon technical report A*, 41(1), 8-16.

51. Jin, Kaiyuan; Krishna, Akshay Bharadwaj; Wong, Zachary; Fisher, Timothy; Ayyaswamy, Portonovo; Catton, Ivan (2022), "Thermohydraulic experimental data for a supercritical carbon dioxide - air microtube heat exchanger ", *Mendeley Data,* V1, doi: 10.17632/mn2wwp9r23.1

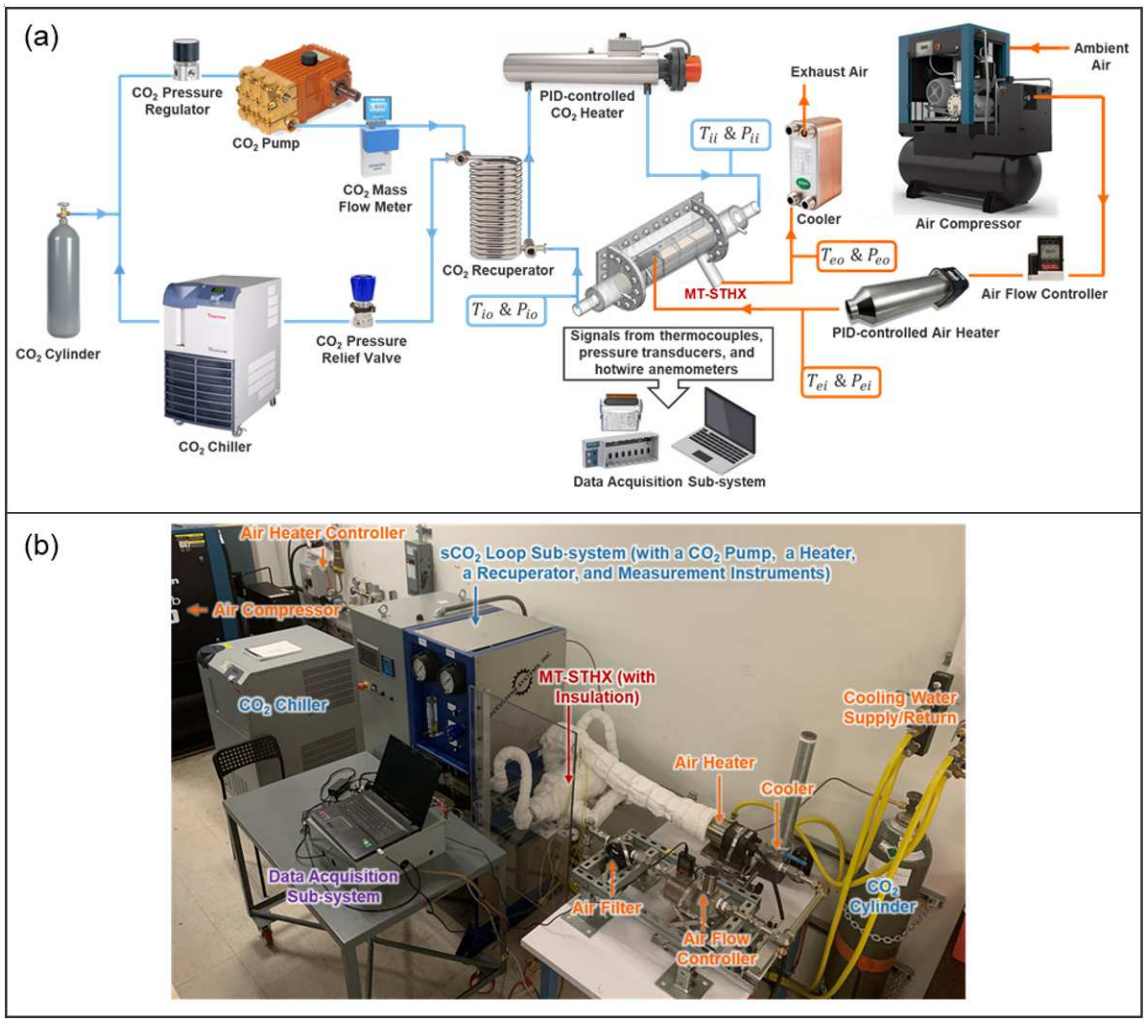

Figure 1. (a) Schematic and (b) picture of the integrated test system for the sCO_2-air MT-STHX.

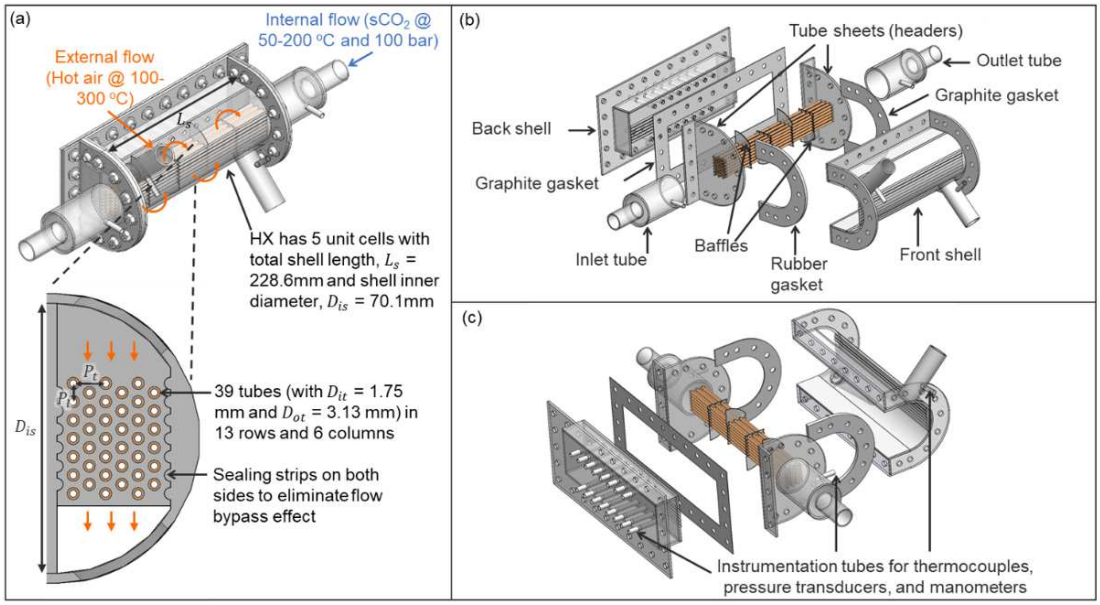

Figure 2. Schematic of the designed and fabricated MT-STHX: (a) 3D schematic of the HX assembly, (b) picture of the HX assembly, (c) 3D schematics in exploded view. (Reproduced with permission [51])

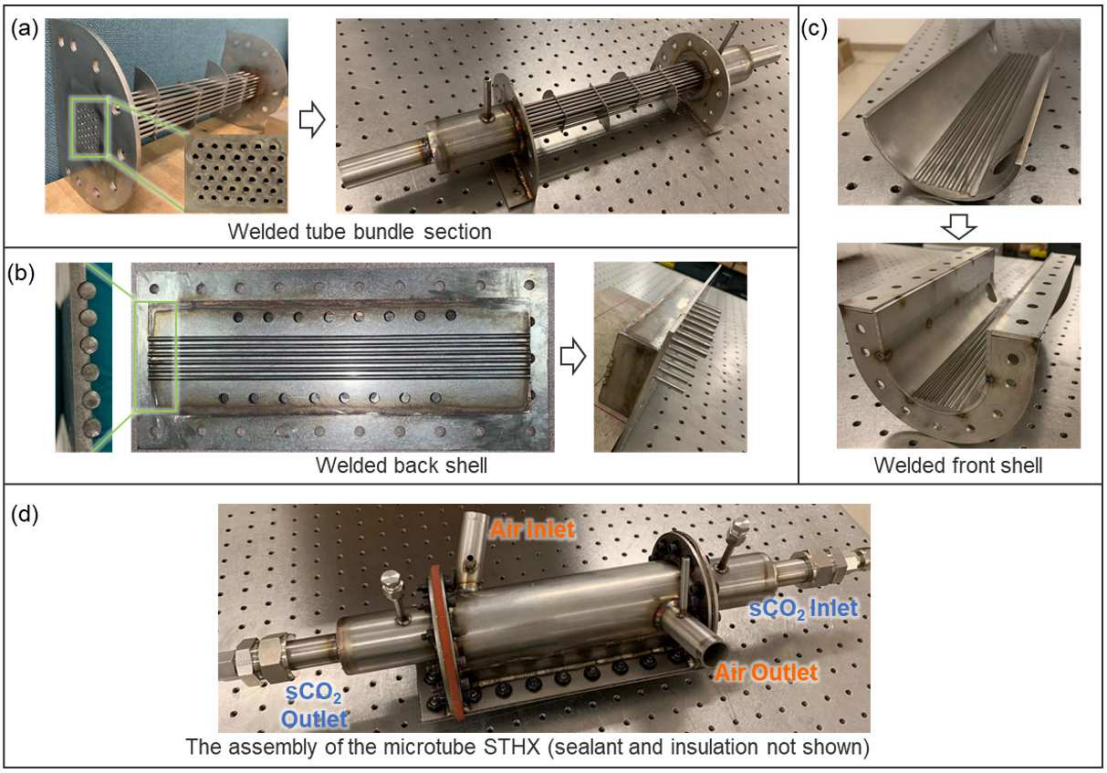

Figure 3. Process flowchart for fabricating (a) the tube bundle section, (b) the back shell, (c) the front shell, and (d) assembling the MT-STHX. (Reproduced with permission [51])

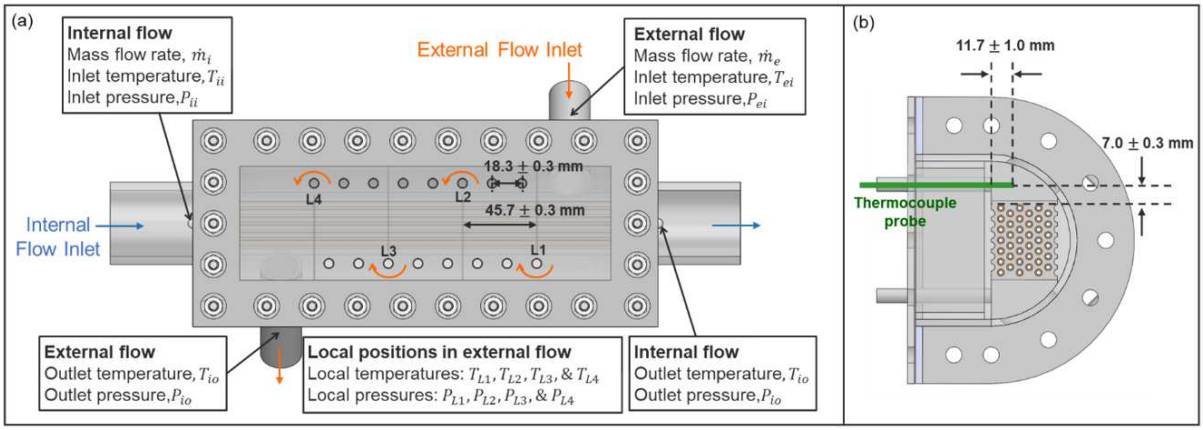

Figure 4. Measured parameters and their locations in the MT-STHX: (a) front view and (b) side view. (Reproduced with permission [51])

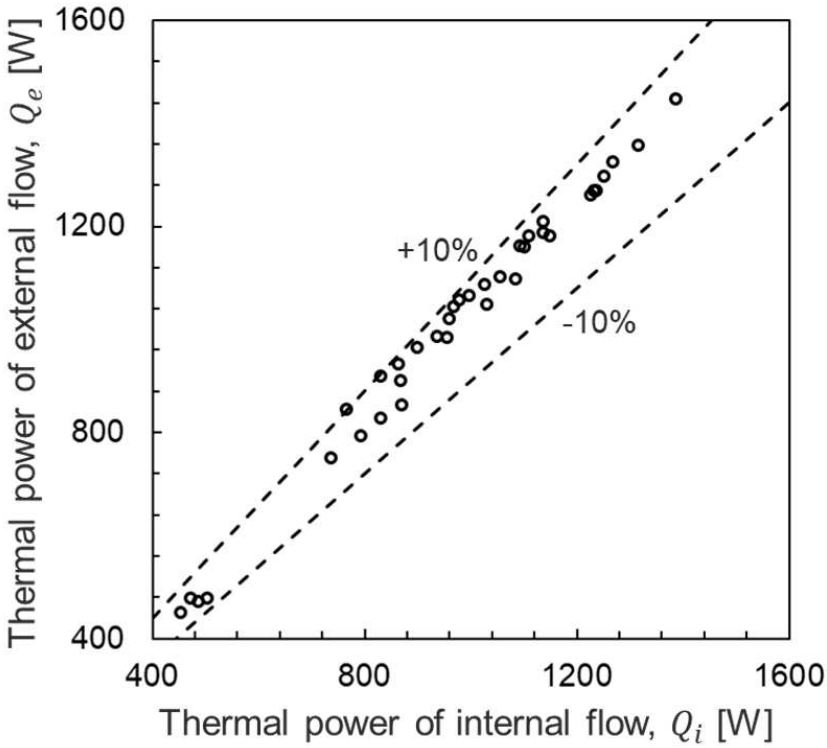

Figure 5. Comparison of thermal power between the internal (sCO_2) and external (air) flow.

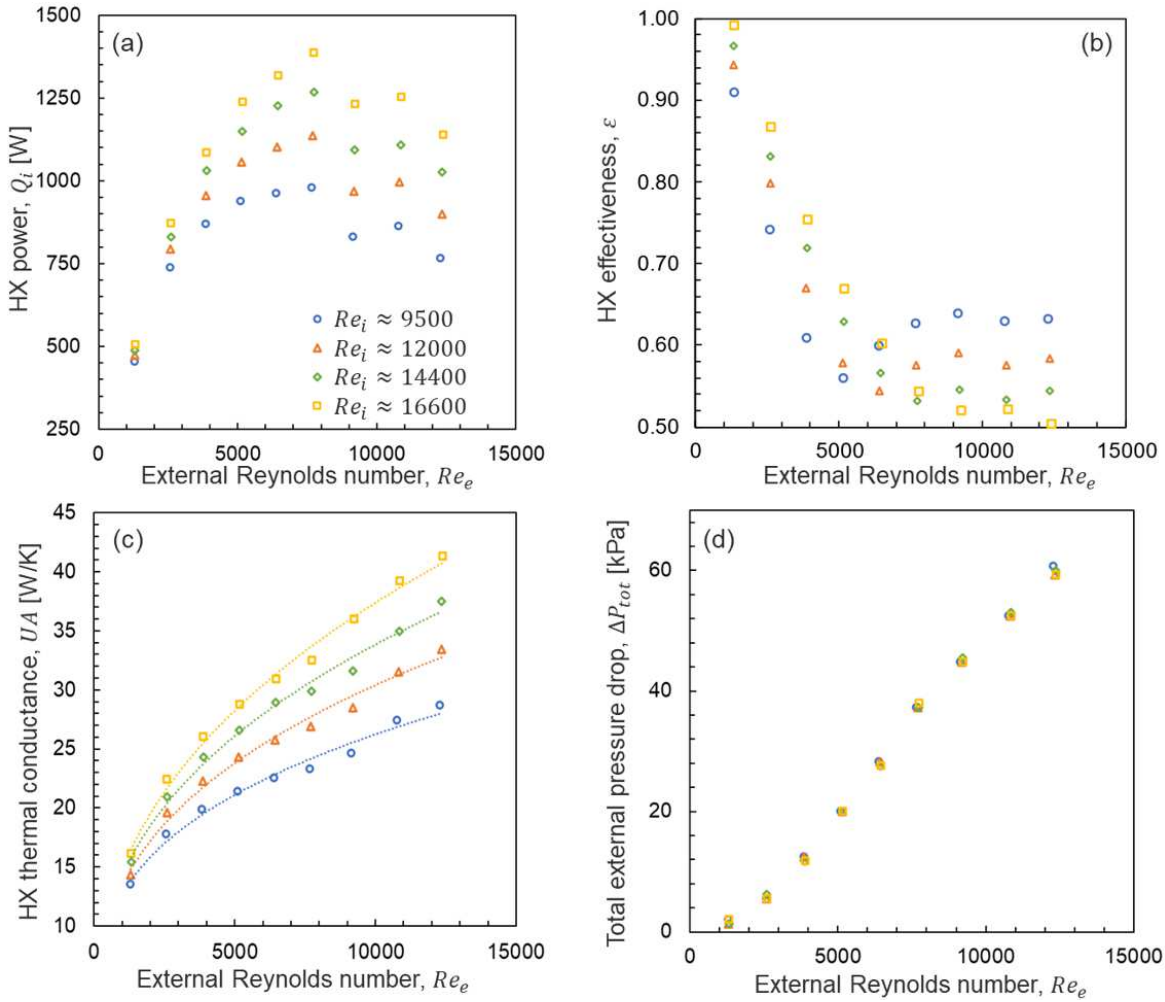

Figure 6. Heat exchanger (a) power (HX capacity), (b) effectiveness, (c) thermal conductance, and (d) total external pressure drop in thermohydraulic tests.

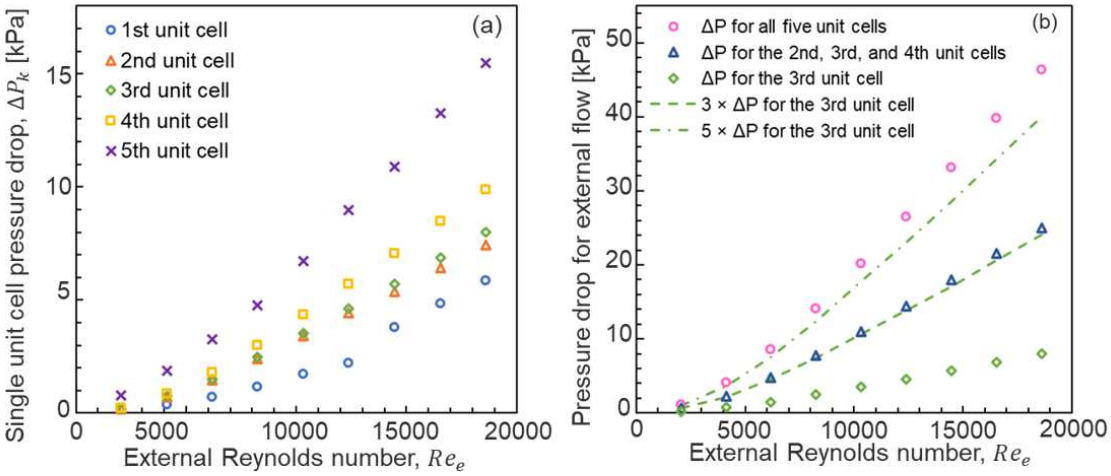

Figure 7. Results from additional hydraulic experiments: (a) single unit cell pressure drops (b) pressure drop comparison among all five cells, central three cells, and the central unit cell.

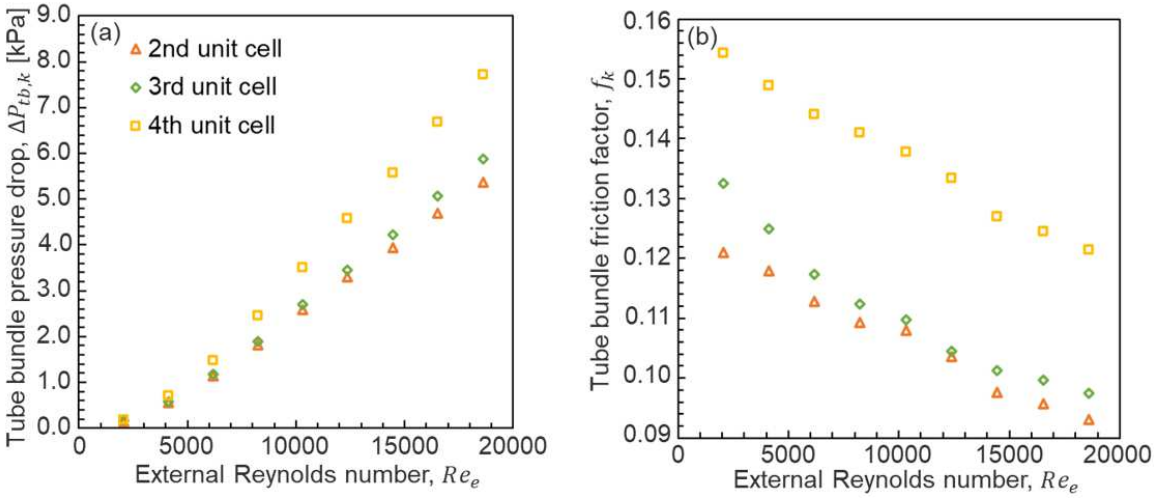

Figure 8. Results from additional hydraulic experiments: (a) tube bundle pressure drops and (b) friction factors for 2nd, 3rd, and 4th unit cells.

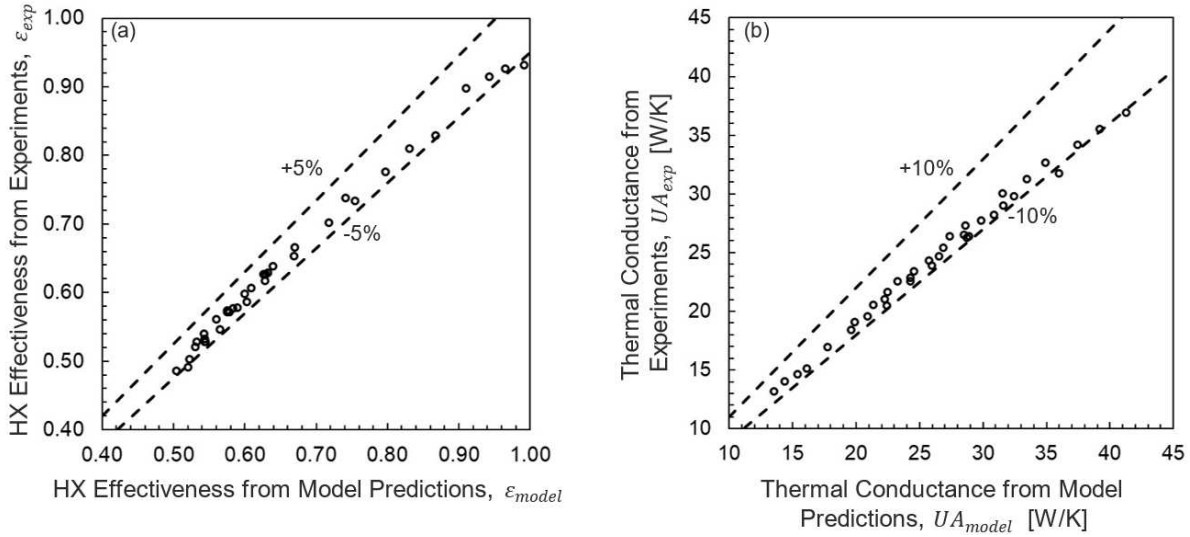

Figure 9. Comparison between experimental and model predictions for (a) HX effectiveness and (b) thermal conductance.

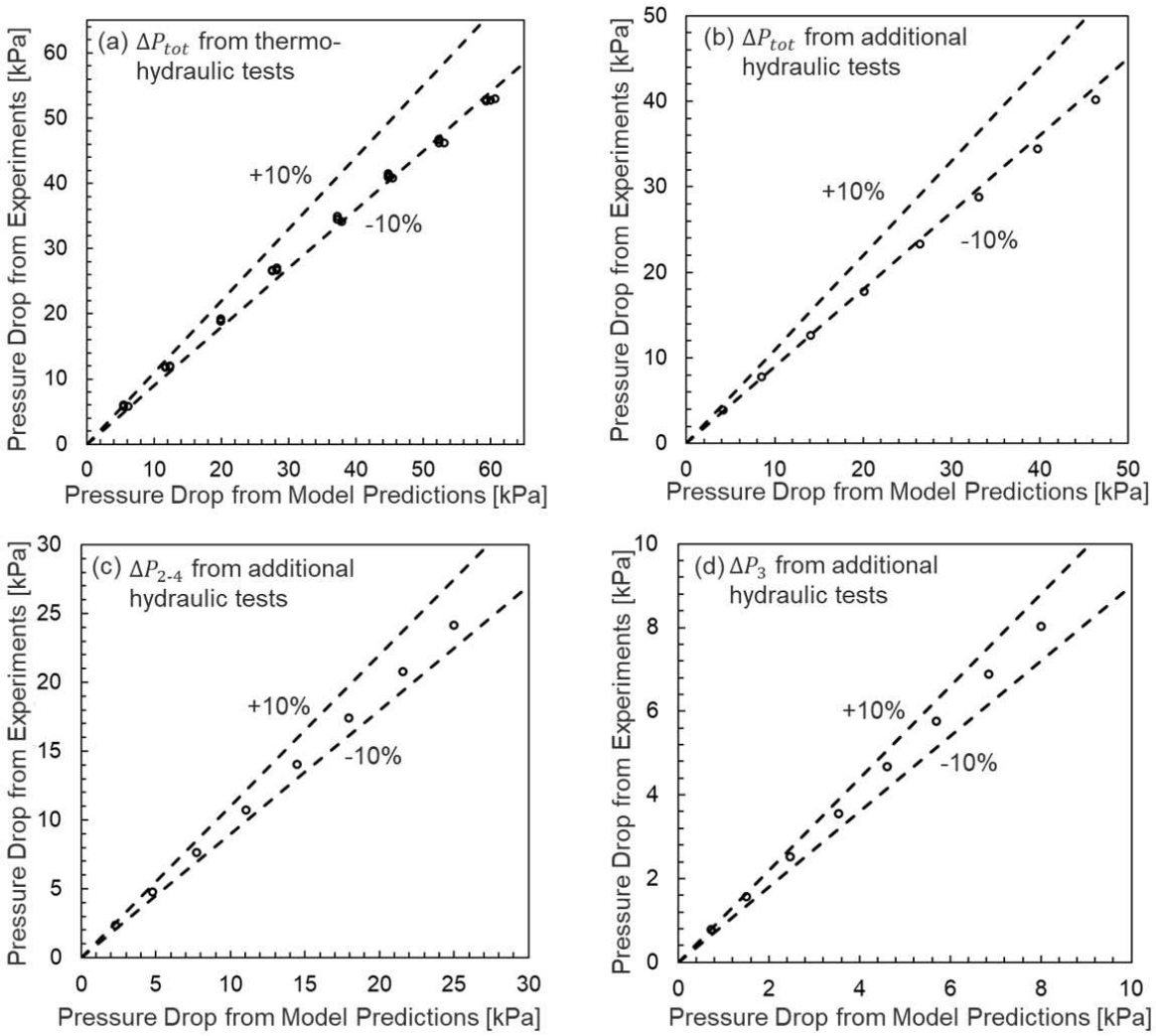

Figure 10. Comparison between experiments and model predictions for (a) total pressure drop in thermohydraulic experiments, (b) total pressure drop in additional hydraulic experiments, (c) pressure drop from 2nd to 4th unit cells in additional hydraulic experiments, and (d) 3rd unit cell pressure drop in additional hydraulic experiments.

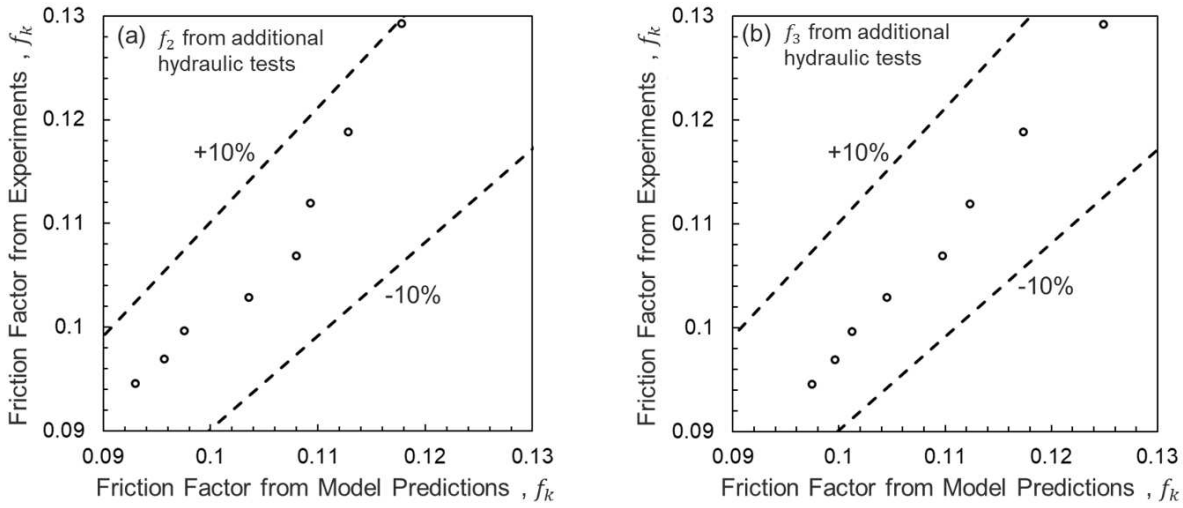

Figure 11. Comparison between experiments and model predictions for (a) 2nd unit cell friction factor (b) 3rd unit cell friction factor.

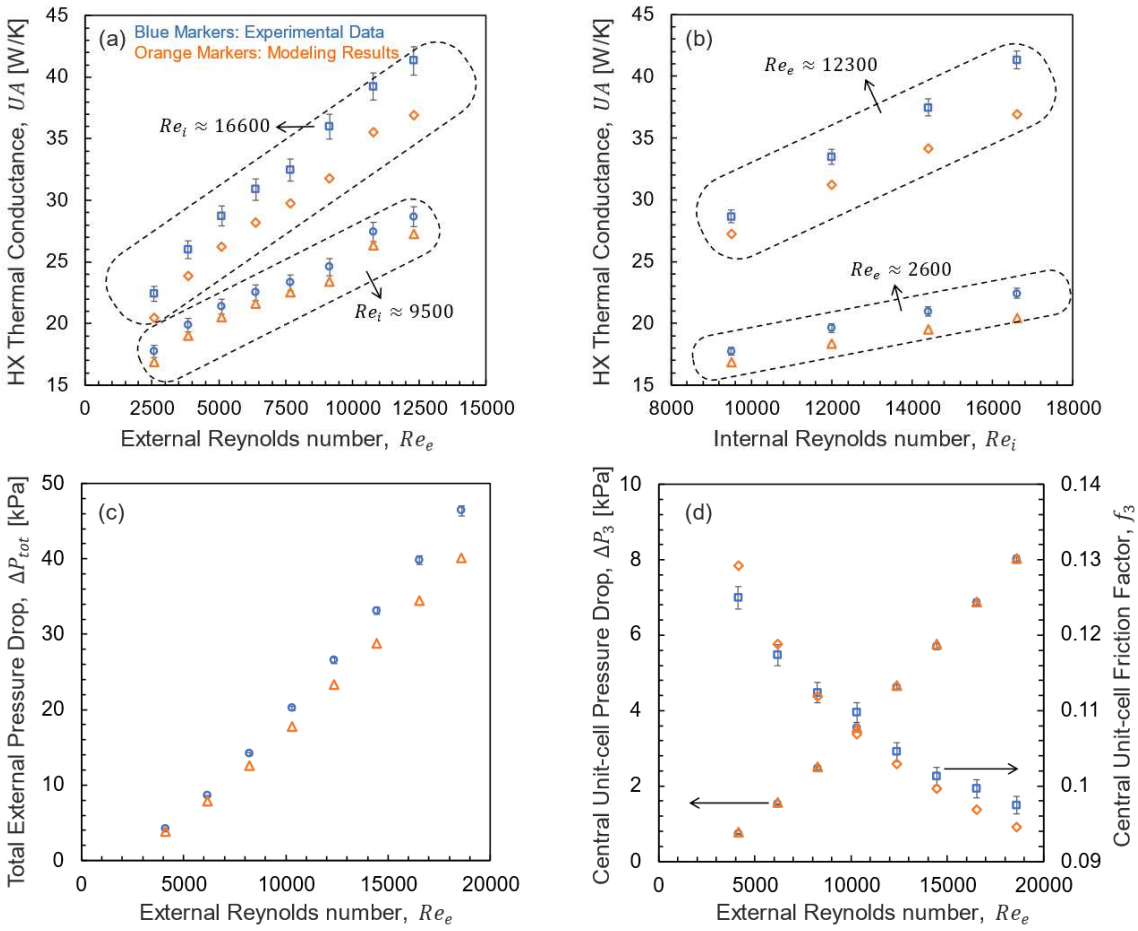

Figure 12. Comparison between experiments and model predictions with various Reynolds numbers: UA relative to external Reynolds number, (b) UA relative to internal Reynolds number, (c) total external pressure drop relative to external Reynolds number, and (d) external pressure drop and friction factor of the central unit-cell relative to external Reynolds number.